Power Electronic Systems
Laboratory

Proceedings of the 31st Applied Power Electronics Conference and Exposition (APEC 2016), Long Beach, CA, USA, March 20-24, 2016

Novel Contactless Axial-Flux Permanent-Magnet Electromechanical Energy Harvester

M. Flankl
A. Tüysüz
I. Subotic
J. W. Kolar

Eidgenössische Technische Hochschule Zürich
Swiss Federal Institute of Technology Zurich

Novel Contactless Axial-Flux Permanent-Magnet Electromechanical Energy Harvester

Michael Flankl[1], Arda Tüysüz[1], Ivan Subotic[2] and Johann W. Kolar[1]

[1]Power Electronic Systems Laboratory
Swiss Federal Institute of Technology (ETH Zurich),
Physikstrasse 3
8092 Zurich, Switzerland

[2]Liverpool John Moores University
School of Engineering,
Byrom Street
Liverpool L3 3AF, UK

***Abstract*—This paper proposes a novel type of watt-range permanent-magnet energy harvester, which harvests energy from a moving conductive body or surface without mechanical contact, as its operation is purely based on eddy-current coupling. The harvester's main advantage over existing solutions is that it allows energy transfer over atypically large (2 ... 15 mm) air gaps, which are unavoidable in certain industrial applications. The paper provides a detailed description of the system's operating principle, and elaborates its modeling using 3-D Finite-Element Method (FEM) analysis. Two prototypes are built and tested for verifying the models. A power of 2.42 W is harvested from an aluminum surface moving with 10 m/s, over 12 mm air gap using a prototype with $\approx 14\,\mathrm{cm}^3$ magnet volume. Moreover, the effects of the harvester's placement as well as the speed of the moving conductive surface on the maximum harvested power and the system's efficiency are analyzed, both with FEM simulations and measurements.**

***Index Terms*—Kinetic energy harvesting, electromagnetic energy harvesting, watt-range energy harvesting, eddy-current coupling, electromagnetic coupling, air gaps.**

NOMENCLATURE

BLDC	Brushless DC
EHS	Energy harvesting system
FEM	Finite-element method
KEH	Kinetic energy harvester
MCS	Moving conductive secondary
MPP	Maximum power point
PM	Permanent magnet
B_r	PM remanent flux density
η_MPP	Efficiency at MPP
φ_1	KEH angle of rotation
$\vec{f}_\mathrm{Lorentz}$	Lorentz force density
g	Air gap
H_cb	PM coercivity
h_m	KEH magnet height
I_1	Generator current
κ	MCS conductivity
k_T1	KEH torque slope
k_P2	MCS power slope
l_ov	Overlap between r_1 and MCS
n_PM	Quantity of PMs
P_1, p_1	Power harvested by KEH (RMS, $p(t)$)
P_2, p_2	Power supplied by MCS (RMS, $p(t)$)
P_ind	Generator input power
P_MPP	Power harvested by KEH at MPP
r_1	KEH PM center radius
r_2	MCS radius
r_m	PM radius
R_gen	Generator phase-to-phase resistance

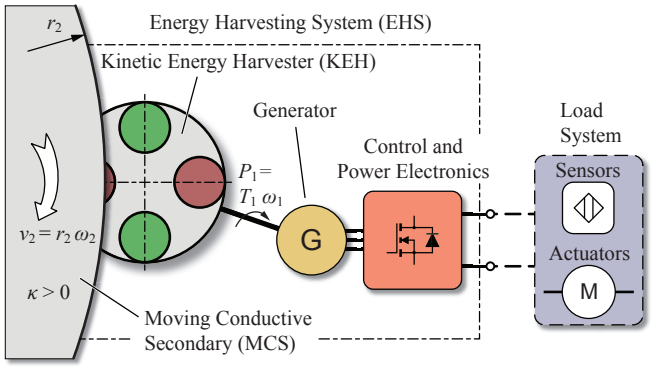

Fig. 1: Overview of the proposed Energy Harvesting System (EHS). Kinetic energy is harvested electromechanically from a moving conductive body (MCS) without mechanical contact and then converted into electrical energy using a generator which supplies a load system through a power electronics interface.

T_1	Electromagnetic torque on KEH
T_2	Torque on MCS
$T_\mathrm{fr+loss}$	Total friction torque and loss torque in generator
T_max	Electromagnetic torque on KEH at $\omega_1 = 0$
v_2	MCS surface speed
ω_1	Angular frequency of KEH
ω_2	Angular frequency of MCS

I. INTRODUCTION

In various fields of industry, remote devices such as wireless sensors [1–3] or actuators require a milliwatt- or watt-range power supply. This is most commonly achieved by employing an energy storage (e.g. batteries), wireless power transfer [4] or a wired connection to a power grid. Nevertheless, occasionally the most practical way of powering such devices is to extract the required power directly from the device's surrounding by using Energy Harvesting Systems (EHS). A diagram of such an EHS with a moving conductive body as energy source is presented in Fig. 1, while Fig. 2 illustrates the realization of the proposed EHS.

Traditionally, the term *energy harvesting* relates to low power levels, ranging from a few microwatts [5–7] to milliwatts [8–12]. However, emerging remote devices such as actuators operating on higher, watt-range power levels cannot be sup-

978-1-4673-9550-2/16/$31.00 ©2016 IEEE

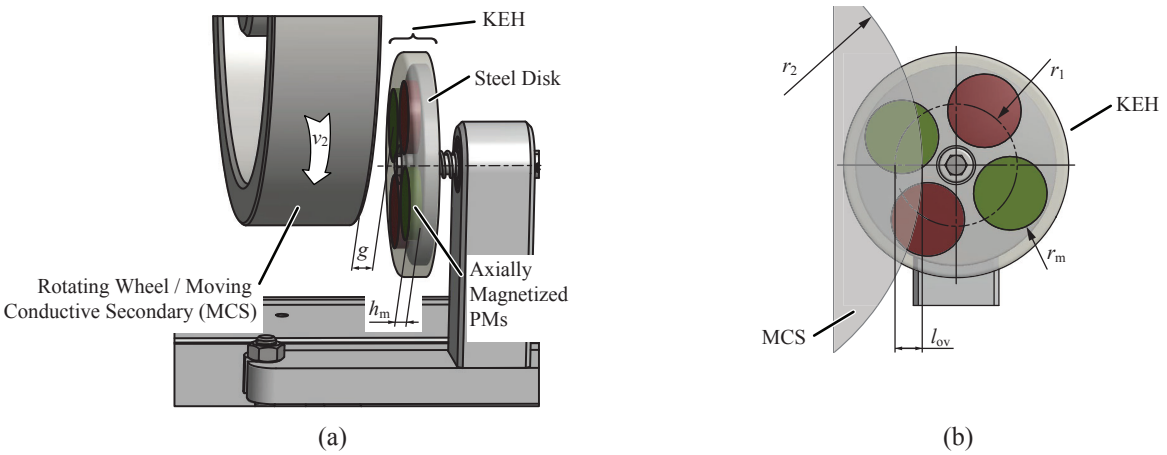

Fig. 2: Kinetic Energy Harvester (KEH), comprising axially magnetized PMs and an iron yoke, rotating in close vicinity of a rotating wheel, i.e. a Moving Conductive Secondary (MCS). Kinetic power is transferred electromechanically over an air gap g between MCS and KEH. (a) shows a side view of the system, illustrating air gap (g) and magnet height (h_m). A projection view of the system in given in (b), where radial dimensions r_1, r_2, r_m and the overlap length l_{ov} are defined.

plied by simple adjustments of existing harvesting topologies. Accordingly, novel energy harvesting methods need to be addressed in research.

A comprehensive overview of well-established low-power kinetic and electromagnetically energy harvesting systems can be found in [13, 14], while a watt-range kinetic EHS for emerging applications has recently been introduced in [15–17] and analyzed in detail in [18]. Power is extracted contactless in an electromagnetic way from a moving conductive body or surface, which will be referred to as Moving Conductive Secondary (MCS) in the following. Fig. 3 shows this EHS, where radially magnetized Permanent Magnets (PMs) are mounted on a magnet wheel (henceforth called the *Kinetic Energy Harvester* (KEH)) that is free to rotate around its axis. The KEH is placed above the MCS, such that its axis of rotation is parallel to the MCS surface. The PM field induces eddy currents in the MCS, and eddy-current coupling takes place between the two mechanical systems, i.e., forces apply both on the KEH and the MCS due to the induced eddy currents. Accordingly, the KEH rotates and drives a generator which converts the kinetic energy of the MCS into electrical energy. The generator may be formed by coils wound directly around the KEH as shown in Fig. 3 [18]; or alternatively, a stand-alone electrical machine can be mechanically coupled to the KEH and be used as a generator. Such an EHS, i.e. the combination of a contactless KEH and a generator could e.g. be used for extracting kinetic energy from a rotating aluminum wheel in order to supply an LED lighting system [15].

In the arrangement of [18] (cf. Fig. 3), the axis of the KEH lies parallel to the MCS surface, which leads to a limited magnetic coupling between PMs and the MCS, as only the PMs that are closest to the MCS interact with it over the narrowest region of the air gap. The rest of the PMs, on the other hand, do not contribute significantly to the magnetic coupling. In order to avoid this drawback, the EHS concept shown in Fig. 1 is proposed in this paper. The proposed EHS features a new KEH arrangement, which is shown in Fig. 2. This new structure consists of a disk which freely rotates around its axis, and axially magnetized PMs placed on its surface facing the MCS. The disk is made of magnetic steel and provides a low-reluctance return path to the PM flux that induces eddy currents in the MCS across the air gap. The steel disk is dimensioned sufficiently thick, such that the guided flux of PMs does not lead to magnetic saturation in it. As its axis of rotation is perpendicular to the MCS, magnets interact with the MCS over a constant air gap. Therefore, a stronger

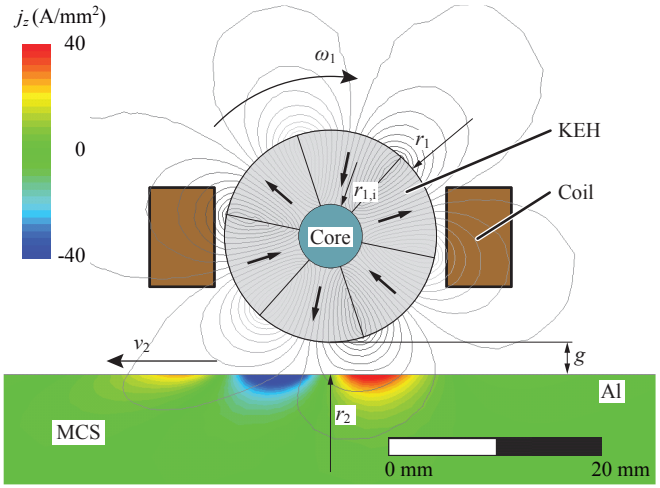

Fig. 3: The EHS analyzed in [18]. Radially magnetized PMs are mounted on a wheel (KEH) that is free to rotate around its axis. The PM field induces eddy currents in the MCS and establishes a contactless eddy-current coupling between the two mechanical systems. The mechanical energy of the KEH wheel may be converted into electrical energy either by coils wound directly around it, or by a mechanical coupling to the shaft of a generator.

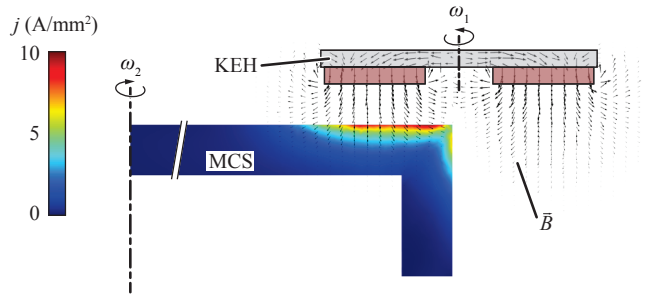

Fig. 4: Cross section of a 3-D FEM simulation. The PM flux, illustrated with an arrow field, induces eddy currents in the moving conductive secondary (MCS). Currents in the MCS are mainly induced in a skin depth in the millimeter-range. Currents and magnetic flux build up Lorentz forces which enable the kinetic energy harvesting.

electromagnetic coupling compared to [18] is achieved.

In order to focus on the new KEH design, in a first step, an off-the-shelf three-phase brushless DC (BLDC) machine is connected mechanically to the disk and employed as the generator.

This paper is about describing the physical operating principle of the presented novel system, its 3-D FEM modeling and the analysis of the influence of the main operation parameters (air gap g, MSC speed v_2 and radial overlap of KEH and MCS l_{ov}) on the system's performance.

The harvester's principle of operation is described and the conducted system modeling is elaborated in Sec. II. Sec. III details the hardware setup with the manufactured harvester prototypes and presents results obtained by measurements and simulations. Sec. III-D focuses on the scaling of harvested power under variation of operation parameters such as air gap (g), MCS speed (v_2) and overlap (l_{ov}), while Sec. IV concludes the paper.

II. Principle of Operation and System Modeling

Eddy-current couplings are a mature technology [19]. They are typically utilized in heavy-duty drivetrains for overload protection and vibration isolation as they are characterized by low maintenance requirements [20]. The functional principle of the KEH shown in Fig. 2 is principally similar to an axial-flux eddy-current coupling. However, in standard eddy-current couplings, the two shafts are usually coaxial in order to maximize the coupling efficiency [21]. On the other hand, in the proposed energy harvesting application, where the energy source is the rotation of a conductive body (e.g. a gear wheel), such coaxial arrangement may not be possible.

Moreover, the MCS movement could be translational instead of rotary, for instance when energy has to be harvested from the translational movement of a conveyor. Therefore, a non-coaxial arrangement with a partial overlap l_{ov} (cf. Fig. 2b) of the KEH and the MCS is considered in this work in order to cover a wider range of energy harvesting applications. For

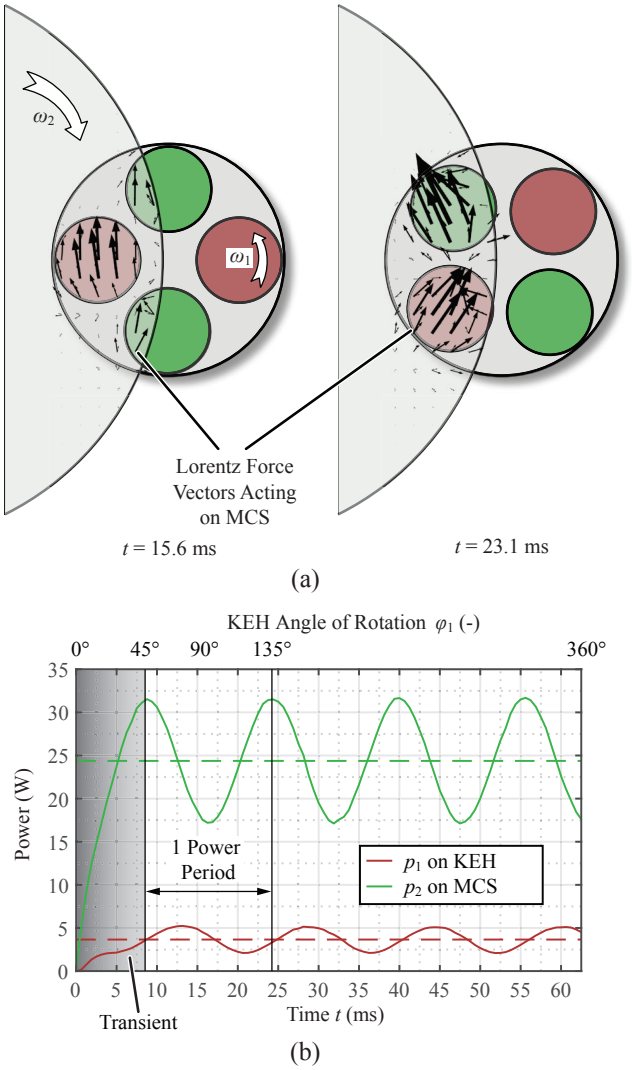

Fig. 5: Build up of torque and power in the energy harvesting system under consideration. The built up Lorentz forces in the MCS are depicted for two different KEH positions in (a) with black arrows as result of a 3-D FEM simulation. Due to the relative speed between KEH magnet field and MCS, eddy currents are induced in the MCS and Lorentz forces are built up. The Lorentz forces describe the power transfer between MCS and KEH. In the figure on the left, a large fraction of the Lorentz force contributes to torque on the KEH. In the right position, the Lorentz force magnitudes are higher, although due to their directions, less effectively contributing to torque on the KEH. The power harvested by the KEH ($p_1(t)$) and the power supplied by the MCS ($p_2(t)$) as outcome of a time-transient 3-D FEM simulation are depicted in (b).

this presented case, computationally efficient analytic models developed for coaxial eddy-current couplings (e.g. [22]) cannot be used, and therefore a FEM-based modeling approach is adopted.

Since the magnetic circuit of Fig. 2 is not continuous in neither a linear nor a rotational axis, a 3-D model is required. Moreover, as the MCS and the KEH are rotating around different axes, the overall system cannot be modeled by only

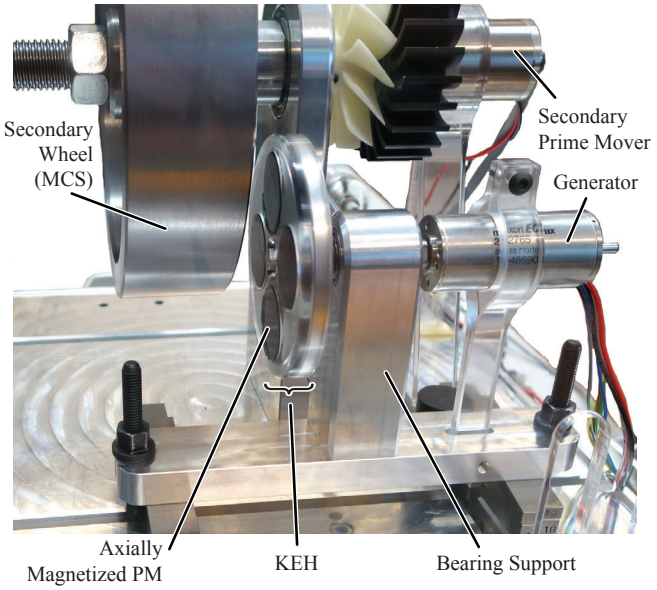

Fig. 6: Test setup of the proposed EHS. The KEH is positioned in the vicinity of the MCS as illustrated in Fig. 2. A DC machine with speed control is employed as prime mover of the MCS. The KEH extracts kinetic power over an air gap and an off-the-shelf BLDC machine is utilized as generator.

TABLE I: TEST SETUP PARAMETERS.

Parameter	**Variable**	**KEH (1)**	**KEH (2)**
KEH PM center radius	r_1	15 mm	25 mm
PM radius	r_m	7.5 mm	15 mm
PM height	h_m	2 mm	5 mm
Steel disk thickness	h_Fe	5 mm	6 mm
Qty. of PMs	n_PM	4	
PM grade		N48M	
PM coercivity[a]	H_cb	1035 A/mm	
PM remanence[a]	B_r	1.4 T	
PMs volume	V_mag	1.4 cm^3	14 cm^3
MCS radius	r_2	100 mm	
MCS length	l_2	45 mm	
MCS thickness	h_2	15 mm	
MCS material		Al: EN AW-6082 (Ac-112)	
MCS conductivity[a]	κ	24...32 MS/m	
MCS permeability	μ_2	μ_0	
MCS surface speed	v_2	5...15 m/s	
Air gap	g	3...15 mm	
Nominal operation parameters			
Air gap	g	3 mm	12 mm
MCS surface speed	v_2	10 m/s	
Overlap	l_ov	10.3 mm	8.7 mm

[a] Datasheet value.

the relative motion of the two mechanical systems, but the true motions of both the MCS and the KEH have to be incorporated in the FEM model by two domains of rotating mesh.

As a first step, only disk-shaped, axially magnetized NdFeB PMs with a remanent flux density of $B_\mathrm{r} = 1.4\,\mathrm{T}$ are considered in the KEH. Eddy-currents in the PMs as well as in the steel disk (cf. Fig. 2a) are neglected. An aluminum wheel with 100 mm radius, 45 mm axial length and 15 mm thickness is used as MCS. The conductivity of aluminum is taken as $\kappa_2 = 28\,\mathrm{MS/m}$ for the FEM simulations, which is the mean value of the tolerance band specified by the manufacturer (cf. Table I).

Unlike in the case of the wound or cage rotors of conventional induction machines, separate guides for flux and current (i.e. teeth made of magnetic steel and copper or aluminum conductors in slots therein) do not exist in the analyzed setup. In Fig. 4, the PM flux and the induced current in the MCS are depicted for a cross section of the system as result of a FEM simulation. It can be seen that current is mainly induced in a skin depth in the millimeter-range. Hence, the force acting on an infinitesimal element of the MCS can be calculated based on the volumetric Lorentz force density

$$\vec{f}_\mathrm{Lorentz} = \vec{j} \times \vec{B}. \tag{1}$$

Accordingly, the primary (KEH) and secondary (MCS) mechanical powers are obtained by the multiplication of the volume integral of the torque-generating force components with the specific rotational frequency

$$p_i\,(t) = \omega_i\,\vec{\mathrm{e}}_{\mathrm{ax},i} \cdot \int\limits_{V_\mathrm{MCS}} (\vec{r} - \vec{r}_{\mathrm{ax},i}) \times \vec{f}_\mathrm{Lorentz}\,\mathrm{d}v\,, \tag{2}$$

where $i \in \{1, 2\}$ denotes KEH or MCS, $\vec{\mathrm{e}}_{\mathrm{ax},i}$ is the unity coordinate vector of the axis around which the torque is calculated and $(\vec{r} - \vec{r}_{\mathrm{ax},i})$ denotes the vector distance of the integration point to the torque axis.

It has been observed that the volume integration of the Lorentz force density shows better numerical stability compared to a torque computation based on the surface integration of the Maxwell's stress tensor, which is a well-known torque calculation method for FEM simulations. On the other hand, a different torque calculation method may be required in applications where the MCS is made of a magnetic material and the calculation of the cogging torque is of importance.

Fig. 5 shows 3-D FEM simulation results for KEH (2) according to Table I with $n_\mathrm{PM} = 4$ magnets. Lorentz force vectors acting on the MCS are depicted in Fig. 5a for two different KEH positions. KEH and MCS powers are plotted in Fig. 5b as a function of time. Since a full mechanical rotation covers 4 power periods, it is sufficient to analyze ${}^{360^\mathrm{o}}/_{n_\mathrm{PM}} = 90^\mathrm{o}$ of KEH rotation only. Moreover, the first 45^o of KEH rotation after the start of the simulation is disregarded as it is dedicated for allowing the numeric solution to reach its steady state.

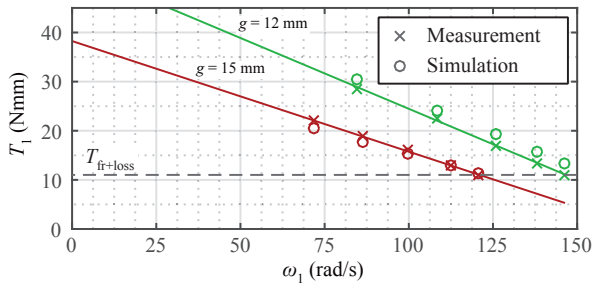

Fig. 7: Torque generation with constant MCS surface speed $v_2 = 10\,\text{m/s}$. Measurements and simulations show that torque is increasing linearly with decreasing rotational frequency of the KEH ω_1 when the MCS surface speed v_2 is kept constant. An increase in air gap g from 12 mm to 15 mm leads to a more flat torque build up curve and consequently to less harvested power. KEH (2) (cf. Table I) is utilized for the measurements/simulations.

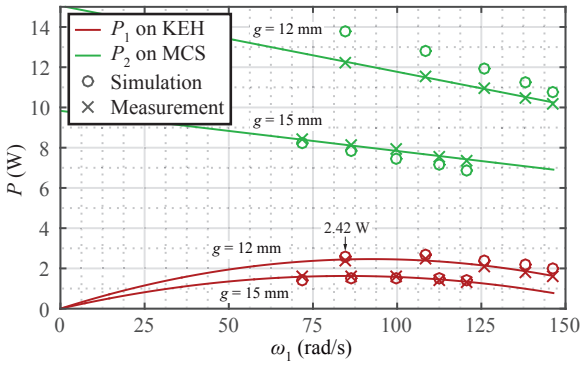

Fig. 8: Measured power extraction with KEH (2) (cf. Table I) for $v_2 = 10\,\text{m/s}$ and $l_{ov} = 8.7\,\text{mm}$. E.g. a remote sensor could be supplied with the extracted power of ($P > 2.4\,\text{W}$), which is harvested over an air gap of $g = 12\,\text{mm}$. 'x' denotes measurement points, solid lines are fitted curves.

III. Test Setup and Measurement Results

Two KEH prototypes are built in order to verify the operating principle qualitatively as well as the 3-D FEM simulations quantitatively. Fig. 6 depicts the hardware test setup with KEH (2) disk (cf. Table I) mounted. Moreover, Table I lists the main parameters of the test setup and the two KEH prototypes. The measurement setup allows to adjust the MCS speed (v_2), the air gap (g) and the overlap (l_{ov}) in wide ranges. An off-the-shelf, three-phase BLDC machine is used as generator. For the measurements conducted in this work, the power electronics interface is omitted and the generator is loaded using a variable resistive load (R_{L}).

A. Harvested Power and Input Power Measurement

Clearly, the harvested power (P_1) and the input power (P_2) are calculated as

$$P_i = T_i \cdot \omega_i \,, \tag{3}$$

with $i \in \{1, 2\}$ denoting KEH and MCS respectively, where rotational frequencies ω_i are measured impulse-based and the torque T_2 on the MCS is measured as reaction torque on the generator with a lever and spring scale system. However, the torque T_1 harvested electromechanically by the KEH cannot be obtained directly in the current setup. Instead, the power and torque harvested by the KEH (P_1 and T_1) are obtained from electrical measurements.

TABLE II: Generator parameters [23].

Parameter	Value
R_{gen}	4.5 Ω
$U_{1,\text{nom}}$	48 V
$I_{1,\text{nom}}$	1.4 A
T_{nom}	64.1 Nmm
ω_{nom}	851.4 rad/s

For an accurate estimation, the losses in the generator and in the bearing support of the KEH (cf. Fig. 6) must be taken into account. Given the RMS voltage U_1 and current I_1 at the generator's terminals, the power input to the generator can be expressed as

$$P_{\text{ind}} = (U_1 + R_{\text{gen}}\, I_1)\, I_1 \,, \tag{4}$$

if the generator coil resistance R_{gen} is known (cf. Table II). Moreover, iron (core) and bearing losses of the generator $P_{\text{l,gen1}}$ must be accounted for. $P_{\text{l,gen1,nom}}$ can be obtained from the generator's datasheet parameters (cf. Table II) for the nominal load point as

$$P_{\text{l,gen1,nom}} = P_{\text{ind,nom}} - T_{\text{nom}}\, \omega_{\text{nom}} \,, \tag{5}$$

with the nominal torque T_{nom} and nominal rotating frequency ω_{nom}. In a simple, yet accurate approach (as will be confirmed later), $P_{\text{l,gen1}}$ is assumed to depend linearly on the rotational frequency. Therefore, an accumulated generator loss torque

$$T_{\text{l,gen}} = {}^{P_{\text{l,gen1,nom}}}\!/_{\omega_{\text{nom}}} = 4.5\,\text{Nmm} \tag{6}$$

is estimated.

$T_{\text{fr}} = 6.5\,\text{Nmm}$ is assumed as the friction torque for the bearings (two bearings of type *608-2Z*) supporting the KEH, according to the bearing manufacturer's data [24]. Therefore, the electrical power measurements are corrected by a total loss torque of

$$T_{\text{fr+loss}} = T_{\text{l,gen}} + T_{\text{fr}} = 11\,\text{Nmm} \,. \tag{7}$$

Finally, the harvested torque is calculated as

$$T_1 = \frac{P_{\text{ind}}}{\omega_1} + T_{\text{fr+loss}} \,. \tag{8}$$

B. Torque and Power Build Up

Simulation and measurement results with two different air gaps are presented in Fig. 7 and Fig. 8. Power extraction of $P_1 > 2.42\,\text{W}$ is achieved with KEH (2) (cf. Table I) over an air gap of 12 mm for a MCS speed of $v_2 = 10\,\text{m/s}$. With the introduced compensation of loss torque on the measurement

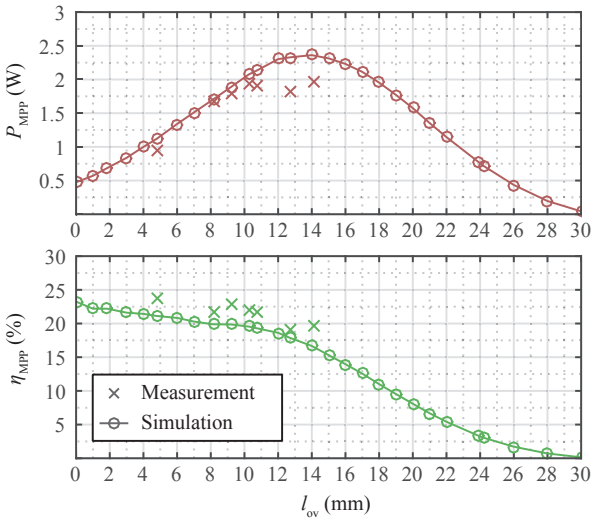

Fig. 9: Influence of overlap (l_{ov}) on the MPP operation. Power and efficiency results for the MPP are extracted according to Sec. III-C from measurements and a total number of 140 3-D FEM simulations. For small overlap values, the coupling between KEH and MCS gradually increases, also P_{MPP} increases, while the efficiency η_{MPP} drops weakly. With the system under consideration, maximum power can be extracted with $l_{\mathrm{ov}} \approx 14\,\mathrm{mm}$ and increasing the overlap further is not favorable since both efficiency and power decrease in this region.

data, it can be observed that measurements and results of 3-D FEM simulations are matching for a range of KEH rotational frequencies ω_1 and air gaps g. Therefore, it can be inferred that the time transient 3-D FEM models described above can be used to model the proposed KEH structure accurately.

C. Maximum Power Point (MPP)

For the further analysis of the given energy harvesting system, it is valuable to analyze the Maximum Power Point (MPP) for a given set of operation parameters (g, v_2, l_{ov}), with respect to the KEH rotating frequency ω_1. Based on the results given in Fig. 7, one can infer that the torque T_1 on the KEH can be modeled as linear function

$$T_1 = T_{\max} - k_{\mathrm{T1}}\,\omega_1\ , \tag{9}$$

where $T_{\max}$ and k_{T1} can be identified by at least two measurements and/or simulations with different ω_1. Similar to the maximum power transfer theorem for linear electric networks, the maximum KEH power can be calculated as

$$P_{\mathrm{MPP}} = \frac{T_{\max}^2}{4\,k_{\mathrm{T1}}}\ . \tag{10}$$

Furthermore, the results depicted in Fig. 8 show that the power input at the MCS can be approximated as a linear function in a similar way,

$$P_2 = P_{2,\max} - k_{\mathrm{P2}}\,\omega_1\ , \tag{11}$$

where $P_{2,\max}$ and k_{P2} are again identified by at least two measurement and/or simulation points with varying ω_1. Finally, the

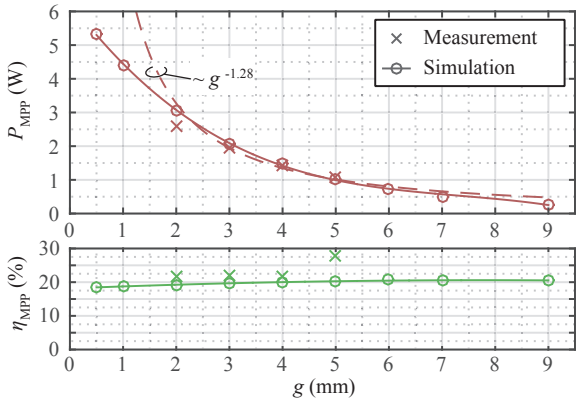

Fig. 10: Influence of air gap on energy harvesting. Clearly, extracted power decreases monotonously with increasing air gap, whereas little influence on efficiency can be observed.

system's efficiency at the MPP can be calculated as

$$\eta_{\mathrm{MPP}} = \frac{T_{\max}^2}{4\,(P_{2,\max}\,k_{\mathrm{T1}} - T_{\max}\,k_{\mathrm{P2}})}\ . \tag{12}$$

D. Impact of Operation Parameters

It is well understood that the width g of the air gap influences the performance of an eddy-current-based electromechanical energy harvester significantly. As shown in [18, 25], the air gap is indeed a limiting factor for electromechanical energy harvesting. As briefly discussed in Sec. II and shown in Fig. 5, different angular rotor positions of the KEH lead to different conditions for torque build up and harvested power. For certain PM positions, it could even occur that insignificant or no power is harvested, while a braking torque acts on the MCS only. Therefore, it is not clear *a priori* how a variation in overlap l_{ov} affects the maximal harvested power P_{MPP} and the efficiency η_{MPP}. In addition, the MCS speed v_2 also influences the harvester operation. In the following, the influence of these operation parameters is analyzed with 3-D FEM simulations and compared to measurements. The smaller prototype KEH (1) with the nominal operation parameters according to Table I is considered in the following, unless otherwise specified.

Both simulations and measurements show that the maximum harvested power P_{MPP} depends on the overlap l_{ov}. The simulation results depicted in Fig. 9 predict a maximum at $l_{\mathrm{ov}} \approx 14\,\mathrm{mm}$. Measurement results agree very well with the simulations up to $l_{\mathrm{ov}} \approx 11\,\mathrm{mm}$, although a discrepancy can be observed around $l_{\mathrm{ov}} \approx 14\,\mathrm{mm}$, which will be investigated in future work.

For $l_{\mathrm{ov}} < 14\,\mathrm{mm}$, the coupling between KEH and MCS gradually increases, also increasing P_{MPP}, while the efficiency η_{MPP} reduces weakly. Above the maximum of P_{MPP}, therefore in the region $l_{\mathrm{ov}} > 14\,\mathrm{mm}$, P_{MPP} decreases again and efficiency η_{MPP} drops significantly. The drop in the efficiency is caused by increasing Lorentz force components

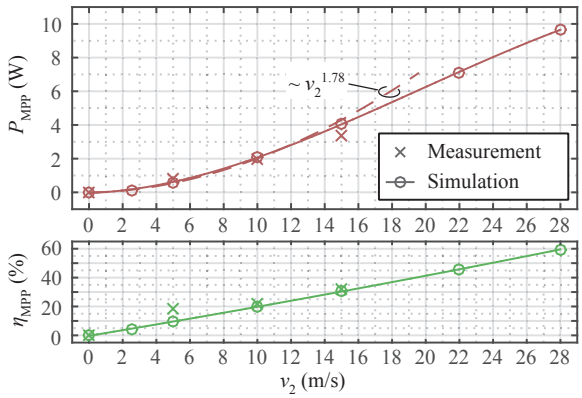

Fig. 11: Influence of MSC surface speed (whose energy sources the harvesting) on the system operation. Extracted power increases stronger than linearly with speed. Both simulations and measurements show that efficiency also increases with speed.

that contribute to the braking torque applying on the MCS, but not to the KEH torque. Consequently, the region slightly below $l_{\mathrm{ov}} \leq 14\,\mathrm{mm}$ can be utilized to resolve the power-efficiency trade-off according to the application at hand.

With the provided hardware setup, measurements in the air gap range $2\,\mathrm{mm} \leq g \leq 5\,\mathrm{mm}$, given in Fig. 10, indicate that the proposed electromechanical energy harvesting is capable of operating with a comparably large air gap. A remarkable power of $P_{\mathrm{MPP}} \approx 1.5\,\mathrm{W}$ can be harvested electromechanically over an air gap $g = 4\,\mathrm{mm}$, which is twice the magnet height $h_{\mathrm{m}} = 2\,\mathrm{mm}$. Simulation results show an estimated power scaling over air gap of $P_{\mathrm{MPP}} \propto g^{-1.28}$ in the air gap range $2\,\mathrm{mm} \leq g \leq 6\,\mathrm{mm}$. This power scaling indicates a better performance for large air gaps of the proposed system in comparison to previously discussed electromechanical energy harvesters, where the harvested power scales with approx. $P \propto g^{-2}$ [18, 25]. With decreasing air gap, i.e. values smaller than the magnet height ($g < 2\,\mathrm{mm}$), P_{MPP} increases less than expected. Air gap reluctance is not dominating the build up of flux for small air gap, but the reluctance path in the MCS limits the generation of Lorentz force and harvested power. For very large air gaps ($g > r_1/2$), harvested power vanishes, since the PM flux closes unfavorably between the magnets in the air gap and not over the MCS. Moreover, it can be observed that air gap hardly affects the efficiency η_{MPP}, as simulations show a variation $< 2\%$ over the investigated air gap range $0.5\,\mathrm{mm} \leq g \leq 9\,\mathrm{mm}$.

As the proposed system harvests the kinetic energy/power of a MCS, its surface speed v_2 clearly affects the level of harvested power. Similar to the previous considerations of overlap l_{ov} and air gap g, simulations and measurements were conducted over a speed range, and results are shown in Fig. 11. For a speed range $v_2 \leq 15\,\mathrm{m/s}$, a scaling $P_{\mathrm{MPP}} \propto v_2^{-1.78}$ is estimated based on simulation results. Also the measurement results are in good accordance with the estimated scaling and simulation results. Surprisingly, a major influence of speed v_2 on the efficiency η_{MPP} can be observed. In the speed range, which is interesting for the proposed harvester, $v_2 \leq 28\,\mathrm{m/s} \approx 100\,\mathrm{km/h}$, a linear scaling of efficiency with speed $\eta_{\mathrm{MPP}} \propto v_2$ is suggested by simulation results. Task of future research is to gain further insight how v_2 affects η_{MPP} and to confirm the simulated efficiency over the full speed range with measurements.

IV. Conclusion

A novel type of Kinetic Energy Harvester (KEH) of a contactless axial-flux permanent-magnet electromechanical Energy Harvesting System (EHS) is presented for watt-range power harvesting from a Moving Conductive Secondary (MCS). The proposed new arrangement of the KEH enhances the magnetic coupling between the harvester and the MCS compared to earlier designs [15–18]. 3-D time-transient FEM models are developed for modeling and optimization of the KEH, and two prototypes are manufactured in order to verify the operating principle qualitatively as well as the FEM simulation models quantitatively. Measurements show a power of $2.42\,\mathrm{W}$ harvested from an aluminum surface moving with $10\,\mathrm{m/s}$, over $12\,\mathrm{mm}$ air gap using prototype KEH (2) with $\approx 14\,\mathrm{cm}^3$ magnet volume.

Simulations and measurements demonstrate that the proposed EHS allows to supply watt-range remote sensors and actuators. Especially the ability of the proposed KEH for harvesting over a wide air gap ($g = 12\,\mathrm{mm}$) allows to encapsulate the system, such that power can be harvested also in harsh industrial environments.

V. Acknowledgment

The authors would like to express their sincere appreciation to Nabtesco Corp., Japan, for the financial and technical support of research on energy harvesting technologies at the Power Electronic Systems Laboratory, ETH Zurich, which provided the basis for achieving the results presented in this paper. In particular, inspiring technical discussions with K. Nakamura and Y. Tsukada are acknowledged. Moreover, the authors acknowledge the support of Comsol Multiphysics GmbH (Switzerland).

References

[1] V. Raghunathan, S. Ganeriwal, and M. Srivastava, "Emerging techniques for long lived wireless sensor networks," *IEEE Communications Magazine*, vol. 44, no. 4, pp. 108–114, April 2006.

[2] R. Vullers, R. Schaijk, H. Visser, J. Penders, and C. Hoof, "Energy harvesting for autonomous wireless sensor networks," *IEEE Solid-State Circuits Magazine*, vol. 2, no. 2, pp. 29–38, Spring 2010.

[3] J. Azevedo and F. Santos, "Energy harvesting from wind and water for autonomous wireless sensor nodes," *IET Circuits, Devices & Systems*, vol. 6, no. 6, pp. 413–420, November 2012.

[4] K. O'Brien, G. Scheible, and H. Gueldner, "Analysis of wireless power supplies for industrial automation systems," *Proceedings of the IEEE Industrial Electronics Society Conference (IECON)*, November 2003.

[5] B. Mack, "Elektromagnetische Energiewandler mit dem Potential zur grossflächigen Anwendung (in German)," Ph.D. dissertation, Albert Ludwigs-Univ. Freiburg, 2009.

[6] H. Lhermet, C. Condemine, M. Plissonnier, R. Salot, P. Audebert, and M. Rosset, "Efficient power management circuit: from thermal energy harvesting to above-IC microbattery energy storage," *IEEE Journal of Solid-State Circuits*, vol. 43, no. 1, pp. 246–255, January 2008.

[7] M. Midrio, S. Boscolo, A. Locatelli, D. Modotto, C. De Angelis, and A.-D. Capobianco, "Flared monopole antennas for 10 μm energy harvesting," in *2010 European Microwave Conference (EuMC)*, September 2010.

[8] T. Krupenkin and J. A. Taylor, "Reverse electrowetting as a new approach to high-power energy harvesting," *Nature Communications*, vol. 2, no. 448, August 2011.

[9] D. Brunelli, C. Moser, L. Thiele, and L. Benini, "Design of a solar-harvesting circuit for batteryless embedded systems," *IEEE Transactions on Circuits and Systems I: Regular Papers*, vol. 56, no. 11, pp. 2519–2528, November 2009.

[10] E. Sardini and M. Serpelloni, "Self-powered wireless sensor for air temperature and velocity measurements with energy harvesting capability," *IEEE Transactions on Instrumentation and Measurement*, vol. 60, no. 5, pp. 1838–1844, May 2011.

[11] Q. Sun, S. Patil, N.-X. Sun, and B. Lehman, "Phase/RMS maximum power point tracking for inductive energy harvesting system," *Proceedings of the IEEE Energy Conversion Congress and Exposition (ECCE)*, September 2015.

[12] J. Moon and S. B. Leeb, "Enhancement on energy extraction from magnetic energy harvesters," *Proceedings of the IEEE Energy Conversion Congress and Exposition (ECCE)*, September 2015.

[13] D. Zhu, S. Beeby, "Kinetic energy harvesting," in *Energy harvesting systems : principles, modeling and applications, ch. 1*. T. J. Kazmierski, S. Beeby, editors, Springer, 2011.

[14] S. Beeby, T. O'Donnell, "Electromagnetic energy harvesting," in *Energy Harvesting Technologies, , ch. 5*. S. Priya, D. J. Inman, editors, Springer, 2009.

[15] D. Strothmann, "Device for contactless current generation, in particular bicycle dynamo, vehicle lighting system and bicycle," DE Patent WO 2013/004 320 A1, January 10, 2013.

[16] Magnic Innovations GmbH & Co KG, checked: 19.11.2015. [Online]. Available: http://www.magniclight.com

[17] Shun-Fu Technology Corp., "Induktionsgenerator," DE Gebrauchsmuster DE 202 014 100 380 U1, 04 24, 2014.

[18] M. Flankl, A. Tüysüz, and J. W. Kolar, "Analysis of a watt-range contactless electromechanical energy harvester facing a moving conductive surface," *Proceedings of the IEEE Energy Conversion Congress and Exposition (ECCE)*, September 2015.

[19] E. Davies, "An experimental and theoretical study of eddy-current couplings and brakes," *IEEE Transactions on Power Apparatus and Systems*, vol. 82, no. 67, pp. 401–419, August 1963.

[20] A. S. Erasmus and M. Kamper, "Analysis for design optimisation of double PM-rotor radial flux eddy current couplers," *Proceedings of the IEEE Energy Conversion Congress and Exposition (ECCE)*, September 2015.

[21] T. Lubin and A. Rezzoug, "3-D analytical model for axial-flux eddy-current couplings and brakes under steady-state conditions," *IEEE Transactions on Magnetics*, October 2015.

[22] J. Wang, H. Lin, S. Fang, and Y. Huang, "A general analytical model of permanent magnet eddy current couplings," *IEEE Transactions on Magnetics*, vol. 50, no. 1, pp. 1–9, January 2014.

[23] Maxon Motor AG, "Datasheet Maxon EC-max 30; 272765," checked: 19.11.2015. [Online]. Available: http://www.maxonmotor.com/medias/sys_master/root/8816804986910/15-227-EN.pdf

[24] SKF Group, "SKF bearing calculator," checked: 19.11.2015. [Online]. Available: http://webtools3.skf.com/BearingCalc/

[25] M. Flankl, A. Tüysüz, and J. W. Kolar, "Analysis and power scaling of a single-sided linear induction machine for energy harvesting," *Proceedings of the IEEE Industrial Electronics Society Conference (IECON)*, November 2015.